The Astrophysical Journal Supplement Series, 280:19 (14pp), 2025 September https://doi.org/10.3847/1538-4365/adf1a9


# Phase II of the LAMOST-Kepler/K2 Survey. II. Time Domain of Medium-resolution Spectroscopic Observations from 2018 to 2023

Mingfeng Qin[1,2], Jian-Ning Fu[1,2,3], Weikai Zong[1,2], Peter De Cat[4], Antonio Frasca[5], Tianqi Cang[1,2], Jiangtao Wang[6], Jianrong Shi[7], Ali Luo[7], Haotong Zhang[7], Hongliang Yan[7], J. Molenda-Żakowicz[8], R. O. Gray[9], and Jiaxin Wang[10]

[1] Institute for Frontiers in Astronomy and Astrophysics, Beijing Normal University, Beijing 102206, People's Republic of China; jnfu@bnu.edu.cn
[2] School of Physics and Astronomy, Beijing Normal University, Beijing 100875, People's Republic of China
[3] Xinjiang Astronomical Observatory, Chinese Academy of Sciences, Urumqi 830011, Xinjiang, People's Republic of China
[4] Royal Observatory of Belgium, Ringlaan 3, B-1180 Brussels, Belgium
[5] INAF—Osservatorio Astrofisico di Catania, Via S. Sofia 78, I-95123 Catania, Italy
[6] CAS Key Laboratory of Optical Astronomy, National Astronomical Observatories, Chinese Academy of Sciences, Beijing 100101, People's Republic of China
[7] Key Lab for Optical Astronomy, National Astronomical Observatories, Chinese Academy of Sciences, Beijing 100012, People's Republic of China
[8] Astronomical Institute of the University of Wrocław, ul. Kopernika 11, 51-622 Wrocław, Poland
[9] Department of Physics and Astronomy, Appalachian State University, Boone, NC 28608, USA
[10] School of Science, Chongqing University of Posts and Telecommunications, Chongqing 400065, People's Republic of China
*Received 2025 April 24; revised 2025 July 8; accepted 2025 July 16; published 2025 August 21*

## Abstract

The LAMOST-Kepler/K2 Medium-Resolution Spectroscopic Survey (LK-MRS) conducted time-domain (TD) medium-resolution spectroscopic observations of 20 LAMOST plates in the Kepler and K2 fields from 2018 to 2023, a phase designated as LK-MRS-I. A catalog of stellar parameters for a total of 36,588 stars, derived from the spectra collected during these 5 yr, including the effective temperature, the surface gravity, the metallicity, the $\alpha$-element abundance, the radial velocity (RV), and $v \sin i$ of the target stars, is released, together with the weighted averages and uncertainties. At a signal-to-noise ratio = 10, the measurement uncertainties are 120 K, 0.18 dex, 0.13 dex, 0.08 dex, 1.9 km s$^{-1}$, and 4.0 km s$^{-1}$ for the above parameters, respectively. Comparisons with the parameters provided by the APOGEE and GALAH surveys validate the effective temperature and surface gravity measurements, showing minor discrepancies in metallicity and $\alpha$-element abundance values. We identified some peculiar star candidates, including 764 metal-poor stars, 174 very metal-poor stars, and 30 high-velocity stars. Moreover, we found 2333 stars whose RV seems to be variable. Using Kepler/K2 or TESS photometric data, we confirmed 371 periodic variable stars among the RV variable candidates and classified their variability types. LK-MRS-I provides spectroscopic data that is useful for studies of the Kepler and K2 fields. The LK-MRS project will continue collecting TD medium-resolution spectra for target stars during the third phase of LAMOST surveys, providing data to support further scientific research.

*Unified Astronomy Thesaurus concepts:* Spectroscopy (1558); Catalogs (205); Surveys (1671); Astronomy databases (83); Fundamental parameters of stars (555)

*Materials only available in the online version of record: machine-readable tables*

## 1. Introduction

The Kepler satellite, launched in 2009 and operational until 2018, successfully carried out the Kepler and K2 missions successively, which involved continuous photometric monitoring of more than 780,000 stars in total (W. J. Borucki et al. 2010; S. B. Howell et al. 2014). The high-precision photometric data obtained from Kepler/K2 have been extensively utilized in diverse scientific domains, including exoplanet detection, stellar astrophysics, Galaxy studies, and investigations of solar system objects (G. Barentsen et al. 2018). Despite the important contributions of photometric data, a comprehensive understanding of stellar properties requires more than photometry alone. An accurate and homogeneous determination of atmospheric parameters, such as that achievable with large spectroscopic surveys, is invaluable for a thorough source characterization (C. C. Worley et al. 2020) and to complement their highly precise light curves collected by space missions.

To this aim, several ground-based spectroscopic observation programs have been developed, such as the APOKASC survey (M. H. Pinsonneault et al. 2014, 2018; A. Serenelli et al. 2017), the LAMOST-Kepler project (hereafter the LK project) (P. De Cat et al. 2015; J.-N. Fu et al. 2020), and the K2-HERMES survey (R. A. Wittenmyer et al. 2018). These surveys aim to provide homogeneous spectroscopic follow-up observations of stars targeted by the Kepler and K2 missions, utilizing multiobject spectrographs capable of observing numerous targets simultaneously. For example, APOKASC uses the high-resolution ($R = 22{,}500$) $H$-band spectrograph with 230 fibers from APOGEE on the Sloan Digital Sky Survey (SDSS) 2.5 m telescope to observe Kepler targets (M. H. Pinsonneault et al. 2014). The LK project utilizes the LAMOST telescope with an effective aperture of $\sim$ 4 m and its 4000 fibers to perform low-resolution ($R \sim 1800$) or medium-resolution ($R \sim 7500$) spectroscopic observations of Kepler and K2 fields (P. De Cat et al. 2015; W. Zong et al. 2018; J.-N. Fu et al. 2020; J. Wang et al. 2020). Similarly, the K2-HERMES survey

employs the HERMES multiobject spectrograph on the 3.9 m Anglo-Australian Telescope, which delivers high-resolution spectra with a resolving power of $R \sim 28{,}000$ in a single exposure, enabling simultaneous observations of up to 360 stars (R. A. Wittenmyer et al. 2018).

The LK project was launched in 2010 (P. De Cat et al. 2015) with the primary goal of conducting low-resolution ($R = 1800$, G. Zhao et al. 2012) spectroscopic observations of the Kepler and K2 fields. It began with the Kepler field in 2012 (LK1; P. De Cat et al. 2015) and later expanded to the K2 field in 2015 (LK2; J. Wang et al. 2020). The spectra and stellar parameters derived from the LK project have been applied by astronomers in a wide range of research areas, including stellar parameter determination, stellar pulsations and asteroseismology, exoplanet studies, stellar magnetic activity and flares, peculiar stars in the Milky Way, and binary star systems (J.-N. Fu et al. 2020). In order to obtain time-domain (TD) spectra for stars in the Kepler and K2 fields, the LK project continues alongside the launch of the LAMOST Phase II survey.

Since 2017 September, the upgrade of LAMOST spectrographs has enhanced the telescope's capabilities with the ability to make medium-resolution ($R = 7500$) spectroscopic observation surveys. This enables the pursuit of wide fields of scientific goals, including binary/multiple star systems, stellar pulsations, star formation, emission nebulae, galactic archeology, exoplanet host stars, and open clusters (C. Liu et al. 2020; H. Yan et al. 2022). Subsequently, in 2018 October, the LK Medium-Resolution Spectroscopic Survey (LK-MRS) was launched (W. Zong et al. 2020, hereafter Paper I). This survey selected 20 observational plates of LAMOST for TD spectroscopic monitoring. A total of 12,860 stars are located in the Kepler field, among which 9262 have been previously observed by the Kepler mission. In addition, 41,425 stars are located in the K2 field, among which 19,540 have been observed by the K2 mission. In total, 53.06% of the targets have been previously observed by either the Kepler or K2 missions. Paper I presents a catalog of stellar parameters derived from 1 yr of observation data, including weighted average values and their associated uncertainties. The study also evaluated the uncertainty in these parameters and discussed the scientific prospects in several key areas.

As discussed in Paper I, the LK-MRS data set has been extensively used since its launch. It has been particularly valuable in the study of multiple star systems, including starspot-modulated eclipsing binaries (Y. Pan et al. 2020, 2024; J. Wang et al. 2024), spectroscopic binaries (B. Zhang et al. 2022), pulsating binaries (M. Jin et al. 2024), and ultracool dwarf comoving companions (A. Rothermich et al. 2024). The data set has advanced asteroseismology, enhancing our understanding of stellar pulsations and internal structures in variable stars (J. Wang et al. 2021; X. Y. Ma et al. 2023; P. Zong et al. 2024). LK-MRS data have also been crucial for investigating stellar activity, shedding light on the evolution of magnetic activity in solar-like stars (S. Mathur et al. 2023), chromospheric activities (H. Han et al. 2023; X. Li et al. 2024), and extreme stellar prominence eruptions (H.-P. Lu et al. 2025). Furthermore, LK-MRS spectra have contributed to determining self-consistent stellar radial velocities (B. Zhang et al. 2021), characterizing Kepler targets using ROTFIT (A. Frasca et al. 2022), and estimating stellar parameters and chemical abundances through Cycle-StarNet (R. Wang et al. 2023). These findings not only demonstrate the significant scientific value of the LK-MRS data set but also emphasize the critical need for its sustained development. The continuing spectroscopic observations in the LK-MRS survey are particularly crucial, as the achieved TD spectroscopic coverage provides an essential foundation for in-depth investigations of variable astrophysical sources.

By 2023 June, LAMOST had completed its second phase of sky surveys, and concurrently, LK-MRS concluded its 5 yr regular survey, referred to as LK-MRS-I. This paper presents the observational results of LK-MRS-I. Section 2 provides a comprehensive overview of the LK-MRS observing strategy, target selection, and the outcomes of LK-MRS-I. Section 3 examines the atmospheric parameters derived from the LASP pipeline of LK-MRS-I, evaluating both measurement and external uncertainties. In Section 4, we identify a number of candidates for peculiar stars, including high-velocity stars, metal-poor stars, and those exhibiting radial velocity (RV) variations. Finally, Section 5 summarizes the key findings of this study.

## 2. LK-MRS Observation Strategy and 5 yr Data

### 2.1. Observation Strategy and Targets of LK-MRS

Since 2018 October, LAMOST has launched its second-phase surveys, which include both a low-resolution spectroscopic survey (LRS) and MRS. The MRS is primarily conducted around the full moon nights, accounting for approximately 50% of the observation time for each lunar month, and is divided into non-TD (NT) and TD modes. The NT MRS mode is designed for large-scale spectroscopic mapping. Each plate is observed once, with three consecutive 1200 s exposures per visit, and the resulting spectra are coadded to improve signal-to-noise ratio (S/N). In contrast, the TD MRS mode aims to monitor spectral variability by repeatedly observing each plate over time. The target stars on each plate remain fixed, and each visit includes three to eight single 1200 s exposures. The same stars are revisited across multiple nights throughout the 5 yr survey (C. Liu et al. 2020). Spectroscopic observations of TD MRS can provide atmospheric parameters for variable stars, facilitating more in-depth studies of these stars (X. Li et al. 2022). They are also of great help in the study of spectroscopic binaries, chromospheric activity variations, and flares (Y. Pan et al. 2020; A. Frasca et al. 2022, 2025). The TD MRS comprises four subprojects, one of which is LK-MRS (Paper I).

To integrate Kepler time-series photometry with TD MRS data and enable extensive large-sample studies of Kepler/K2 targets, LK-MRS has strategically selected four observational plates within the Kepler field and 16 plates in the K2 fields, for a total of 20 plates (Paper I). For each plate, the set of target stars is fixed, and repeated spectroscopic observations are scheduled to monitor variability. Each plate is planned for 60 visits, with their spatial distribution indicated by the blue and red circular footprints in Figure 1. All selected plates are positioned above a decl. of $-10^{\circ}$ to ensure that they remain within LAMOST's observable ranges. The limiting magnitude is set at $G = 15.0$ mag, making these stars viable for observation during full moon nights. For a comprehensive description of the target selection methods applied in LK-MRS, see Paper I.

### 2.2. Data of LK-MRS-I

LK-MRS-I conducted TD spectroscopic observations from 2018 September to 2023 June, covering both the Kepler and

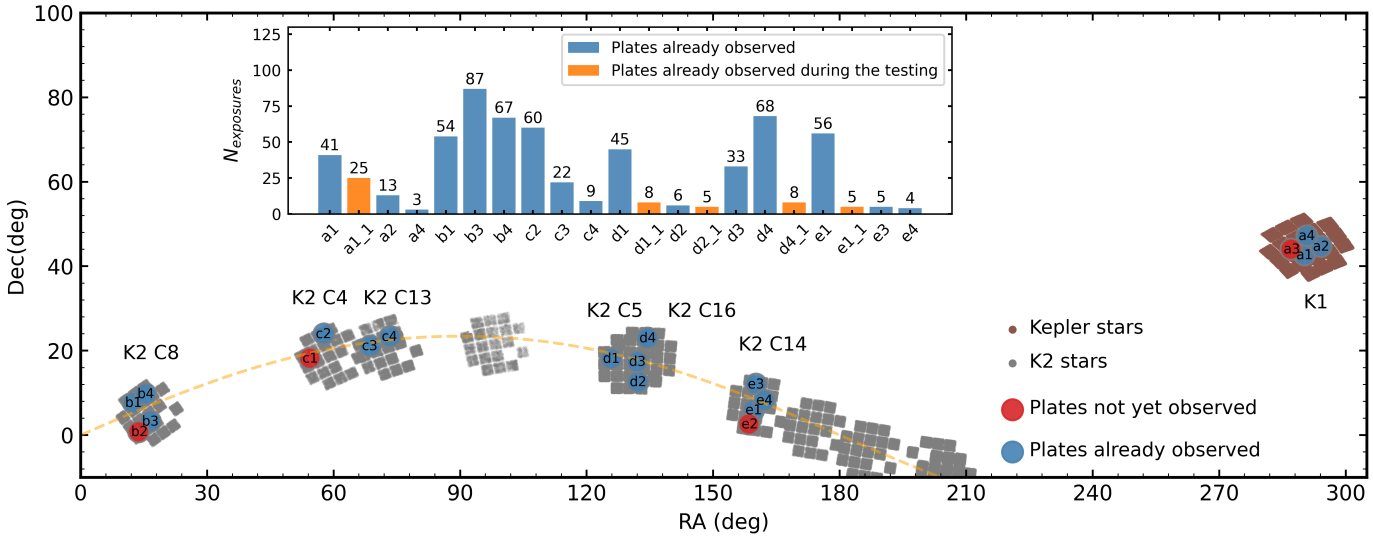


**Figure 1.** Spatial distribution of plates of LK-MRS-I. The yellow dashed line represents the ecliptic plane. The inset shows the exposure counts for each plate. Blue bars represent plates that have been observed, while orange bars indicate plates observed during the testing phase.

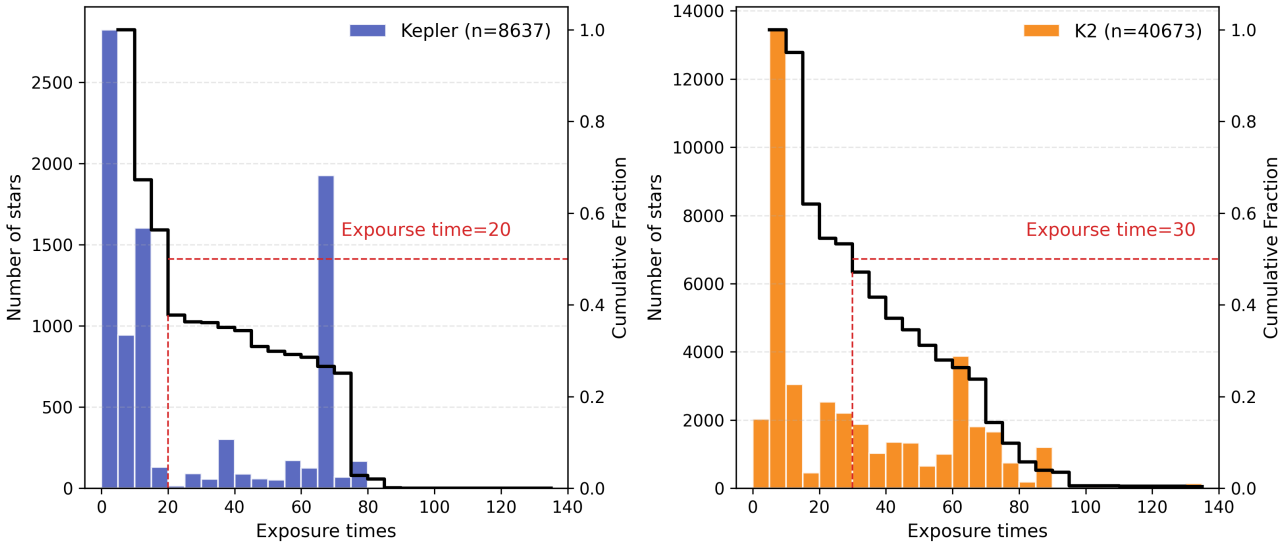


**Figure 2.** Distribution of exposure times for LK-MRS-I sources in the Kepler (left) and K2 (right) surveys. The histogram (vertical bars) shows stellar counts per exposure bin, while the stepped curve (black) displays the reverse CDF computed from the maximum exposure time downward (i.e., fraction of stars with exposure time $\geqslant t$). The red dashed line indicates the median exposure (50th percentile), with its numerical value annotated in the plot.

K2 fields. The distribution of all observed plates in the celestial coordinate system is shown in Figure 1. In this figure, the filled blue circular markers represent plates that have already been observed, while the filled red circular markers indicate plates that have not yet been observed. As of 2023 June, only four plates remain unobserved, three located in the K2 fields and one in the Kepler field. The inset in Figure 1 presents a histogram of the exposure counts for each plate, with blue bars representing 16 of the plates planned for observation in Table 1 of Paper I and orange bars representing the five plates from the testing phase.[11] The inset shows that for four plates, 60 or more observations have been made, while another four already have more than 40 observations. In total, 624 exposures were obtained, completing approximately 52% of the planned observations.

Each exposure produces two single-exposure spectra, one from the red arm and another from the blue arm of the spectrograph. In most cases, three consecutive exposures of the same target are coadded to improve the S/N, resulting in coadded red-arm and blue-arm spectra. LK-MRS-I yielded 3,531,785 spectra, including 2,941,929 single-exposure spectra and 589,856 coadded spectra. These spectra correspond to 49,310 unique stellar targets, comprising 8637 stars in the Kepler field and 40,673 in the K2 field. The distribution of the number of exposures per star is illustrated in Figure 2. The blue-purple bars and orange bars represent the histograms of exposure counts for all stars, 8637 stars in the Kepler fields,

[11] The plan IDs for these plates are HIP95119KP01, TD082325N180811K02, TD084844N123545K02, TD085754N225914K02, and TD103827N055449K02, which correspond to the same fields as K1a1, K2d1, K2d2, K2e1, and K2d4, respectively. We refer to them as K1a1_1, K2d1_1, K2d2_1, K2e1_1, and K2d4_1 in this paper.

**Table 1**
Overview of LK-MRS-I Data

| Year (1) | $N_{\rm plate}$ (2) | $N_{\rm exposures}$ (3) | $N_{\rm spectra}$ (4) | $N_{T_{\rm eff}}$ (5) | $N_{\log g}$ (6) | $N_{\rm [Fe/H]}$ (7) | $N_{\rm RV}$ (8) | $N_{v\sin i}$ (9) | $N_{\rm [\alpha/M]}$ (10) |
|---|---|---|---|---|---|---|---|---|---|
| 2018 | 25 | 136 | 791,779 | 34,211 | 34,211 | 34,211 | 32,377 | 4557 | 18,572 |
| 2019 | 40 | 201 | 1,111,398 | 48,905 | 48,905 | 48,905 | 46,199 | 6412 | 23,846 |
| 2020 | 34 | 142 | 865,996 | 48,263 | 48,263 | 48,263 | 45,619 | 7360 | 27,309 |
| 2021 | 14 | 63 | 357,414 | 17,531 | 17,531 | 17,531 | 16,454 | 2525 | 11,012 |
| 2022 | 11 | 41 | 191,438 | 12,679 | 12,679 | 12,679 | 12,001 | 1628 | 7892 |
| 2023 | 10 | 41 | 213,760 | 9048 | 9048 | 9048 | 8620 | 1328 | 5444 |
| Total | 134 | 624 | 3,531,785 | 170,637 | 170,637 | 170,637 | 161,270 | 23,810 | 94,075 |

**Note.** Column (1) represents the year of observation, column (2) shows the number of plates observed each year, column (3) displays the number of visits per plate annually, column (4) indicates the total spectra observed each year, and columns (5) to (10) denote the count of stellar parameters derived using LASP annually.

and 40,673 stars in the K2 field, respectively. The cumulative distribution functions (CDFs) for all three samples are overplotted to facilitate comparison. In addition, the red dashed line indicates the average number of exposures, which is 20 and 30. The number of exposures in the Kepler field is significantly lower than in the K2 field, mainly because the Kepler observations fall in the summer season, during which LAMOST undergoes regular maintenance in July and August. Additionally, frequent rainfall during summer further reduces observational efficiency.

Among the 589,856 coadded spectra collected, half correspond to blue-arm coadded spectra and the other half to red-arm coadded spectra. Due to the limitations of the LAMOST Stellar Parameter Pipeline (LASP), which is capable of deriving stellar parameters only for late A- and FGK-type stars, stellar atmospheric parameters were successfully determined for 170,637 spectra. Their physical parameters, including effective temperature ($T_{\rm eff}$), surface gravity ($\log g$), and metallicity ([Fe/H]), were derived using the latest version of the LASP pipeline.[12] A summary of annual observations, including the number of plates, exposures, collected spectra, and parameter statistics, is provided in Table 1.

This work presents a statistical analysis of LK-MRS based on the LAMOST DR11[12] data set, covering observations from 2018 September to 2023 June. Compared to Paper I, which only included data from a limited time span (2018 September–2019 June), the current study incorporates four additional years of observations. The early data included in Paper I have been fully reprocessed using the latest version of the LASP pipeline, resulting in improved calibration accuracy and enhanced consistency across the entire data set. The current data set includes 401 additional plate exposures and 2,366,133 more spectra relative to Paper I. These additions not only contribute new stellar targets but also provide new epochs for previously observed stars, significantly improving the temporal coverage for TD analysis. Therefore, the current release offers both new detections and improved measurements relative to Paper I, enabling more robust statistical and variability studies.

## 3. Stellar Atmospheric Parameters of LK-MRS-I

### 3.1. Atmospheric Parameter Catalog of LK-MRS-I

The LASP is an automated pipeline that determines stellar atmospheric parameters, such as $T_{\rm eff}$, $\log g$, [Fe/H], and RV, by matching observed spectra with ELODIE templates.[13] During the LK-MRS-I survey, LASP derived stellar parameters from 170,637 coadded spectra. These spectra correspond to 36,588 unique stars. The difference arises because many stars were observed multiple times over the course of the survey to support TD analyses, and each valid coadded spectrum was processed independently. Specifically, 17,996 stars have at least three valid coadded spectra, enabling variability and rotational studies. In addition to the core LASP parameters, projected rotational velocities ($v\sin i$) were derived using PHOENIX templates (F. Zuo et al. 2024), limited to stars with $T_{\rm eff}$ between 5000 and 8500 K due to resolution constraints, resulting in 23,810 $v\sin i$ measurements. However, we note that, as shown by A. Frasca et al. (2022), $v\sin i$ values smaller than 8 km s$^{-1}$ cannot be reliably derived due to the resolution and sampling of MRS spectra, and only an upper limit of 8 km s$^{-1}$ can be provided in these cases. 94,075 $[\alpha/M]$ measurements were derived in LK-MRS-I. Similarly, 161,270 RV measurements were obtained by matching the spectra with Kurucz templates (R. Wang et al. 2019).

To estimate each stellar parameter, we used Equation (1) from Paper I to compute a weighted mean across multiple observations, yielding the final value of

$$\overline{P} = \frac{\sum_k w_k \cdot P_k}{\sum_k w_k}, \tag{1}$$

where $k \in [1, N]$ denotes the observation index for parameter $P$ of an individual star. The weighting factor $w_k$ is calculated based on the square of the S/N for each analyzed spectrum, thus giving greater importance to the spectra with higher S/N. We also applied Equation (2) from Paper I to calculate the weighted standard error for each parameter,

$$\sigma_w(\overline{P}) = \sqrt{\frac{N}{N-1} \cdot \frac{\sum_k w_k \cdot (P_k - \overline{P})^2}{\sum_k w_k}}, \tag{2}$$

where $\sigma_w(\overline{P})$ represents the standard error of the weighted mean $\overline{P}$. The final parameter values, their standard errors, and the number of observations for each star are summarized in Table 2. The methodology for computing the mean stellar parameters follows exactly the same approach as described in Paper I. However, all spectra used in this work have been reprocessed using the updated LASP pipeline from LAMOST

[12] https://www.lamost.org/lmusers/

[13] http://www.lamost.org/dr11/

**Table 2**
Stellar Atmospheric Parameters Provided by LK-MRS-I

| Times | UID | KIC/EPIC | R.A. (deg) | Decl. (deg) | $T_{\rm eff}$ (K) | log $g$ (dex) | [Fe/H] (dex) | [$\alpha$/M] (dex) | RV (km s$^{-1}$) | $v \sin i$ (km s$^{-1}$) | Label |
|---|---|---|---|---|---|---|---|---|---|---|---|
| (1) | (2) | (3) | (4) | (5) | (6) | (7) | (8) | (9) | (10) | (11) | (12) |
| 12 | G17096966435490 | 220550719 | 10.580750 | 7.910431 | 5645.88 | 4.31 | −0.04 | 0.09 | −2.70 | ⋯ | ⋯ |
| | | | | | ±39.79 | ±0.06 | ±0.03 | ±0.02 | ±0.41 | ⋯ | ⋯ |
| 1 | G16297522311478 | 211440152 | 130.672740 | 12.248783 | 6477.13 | 4.12 | −0.09 | ⋯ | 12.54 | ⋯ | ⋯ |
| | | | | | ⋯ | ⋯ | ⋯ | ⋯ | ⋯ | ⋯ | ⋯ |
| 1 | G16342182680148 | 212019272 | 134.722330 | 20.573745 | 5704.37 | 4.03 | −0.20 | ⋯ | 49.22 | 46.20 | ⋯ |
| | | | | | ⋯ | ⋯ | ⋯ | ⋯ | ⋯ | ⋯ | ⋯ |
| 1 | G16346217356100 | 211524166 | 131.273770 | 13.479998 | 5540.67 | 3.80 | −0.51 | 0.20 | 40.83 | ⋯ | ⋯ |
| | | | | | ⋯ | ⋯ | ⋯ | ⋯ | ⋯ | ⋯ | ⋯ |
| 6 | G16353924667769 | 211833343 | 133.371240 | 17.788899 | 4784.41 | 2.87 | −0.34 | 0.07 | 25.87 | ⋯ | ⋯ |
| | | | | | ±12.74 | ±0.03 | ±0.00 | ±0.01 | ±0.97 | ⋯ | ⋯ |
| 2 | L16715670508803 | 247247018 | 69.458066 | 20.067119 | 4675.25 | 4.63 | −0.67 | ⋯ | 79.24 | ⋯ | ⋯ |
| | | | | | ±0.07 | ±0.01 | ±0.02 | ⋯ | ±0.03 | ⋯ | ⋯ |
| 11 | G17066013434593 | 220491346 | 12.628243 | 6.568253 | 5058.15 | 3.74 | −0.18 | 0.20 | −14.92 | 33.64 | ⋯ |
| | | | | | ±10.18 | ±0.02 | ±0.01 | ±0.02 | ±0.53 | ±3.30 | ⋯ |
| 3 | L16700197857117 | 210867214 | 66.611719 | 20.886968 | 6094.06 | 4.29 | −0.57 | 0.15 | 7.52 | ⋯ | ⋯ |
| | | | | | ±14.52 | ±0.03 | ±0.08 | ±0.07 | ±0.54 | ⋯ | ⋯ |
| 9 | G16342062317845 | 212066917 | 133.435470 | 21.399934 | 5915.86 | 4.20 | 0.00 | −0.05 | −19.21 | ⋯ | RVV |
| | | | | | ±122.62 | ±0.15 | ±0.03 | ±0.02 | ±20.20 | ⋯ | ⋯ |
| 1 | G16340116868661 | 211953970 | 132.402140 | 19.532971 | 5283.99 | 4.10 | −0.58 | ⋯ | 31.29 | ⋯ | ⋯ |
| | | | | | ⋯ | ⋯ | ⋯ | ⋯ | ⋯ | ⋯ | ⋯ |

**Note.** Column (1) provides the number of available spectral parameters for each target, while columns (2) and (3) provide the UID of LAMOST and a combined identifier (EPIC/KIC), respectively. Columns (4) and (5) list the R.A. and decl. of the stars in J2000.0. Columns (6)–(11) present the stellar parameters, including $T_{\rm eff}$, log $g$, [Fe/H], [$\alpha$/M], RV, and $v \sin i$, with their corresponding uncertainties listed below each value. The final column includes classifications or additional comments about the stars. Missing values are denoted by "⋯."

(This table is available in its entirety in machine-readable form in the online article.)

DR11, which incorporates improvements in calibration and parameter estimation. Moreover, the data set used in this study includes four additional years of observations compared to Paper I, resulting in more spectra and higher observation counts for many stars. As a result, while the weighted mean parameters are generally consistent with those in Paper I, small differences may arise due to the inclusion of new measurements and the updated pipeline processing.

Table 2 includes information for a total of 36,588 stars, of which 18,892 stars are listed in the Kepler/K2 input catalogs (STScI 2011, 2016a, 2016b, 2016c), accounting for approximately 51.6% of the total. The first column indicates the number of observation times. The second column lists the unique observation IDs (UIDs) assigned by LAMOST, while the third column provides the corresponding IDs from the Kepler or K2 input catalogs, matched using a crossmatching radius of 3.″7.[14] In cases where multiple Kepler/K2 targets fall within this matching radius, we selected the closest counterpart as the optimal match. IDs greater than 201,000,000 indicate targets from the K2 input catalog, while those less than 201,000,000 belong to the Kepler input catalog. Blank entries in column (3) denoted by "⋯" indicate stars not included in either catalog. The fourth and fifth columns present the R.A. and decl. of the stars in J2000.0. Columns (6)–(11) list the stellar parameters, including $T_{\rm eff}$, log $g$, [Fe/H], [$\alpha$/M], RV, and $v \sin i$, with uncertainties provided below each value. The final column includes classifications or additional comments about the stars, further detailed in Section 4. Missing values or parameters not determined by LASP are also denoted as "⋯", in addition to the case described for column (3). The entire table is published online in a machine-readable format.

### 3.2. Measurement Uncertainties of the Parameters of LK-MRS-I

For stars with multiple spectra measured by LASP, we conducted an assessment of their measurement uncertainties. This was achieved by calculating the difference between the parameters provided by each individual spectrum and the corresponding weighted average parameters, denoted as $\Delta P$, using Equation (3) from Paper I:

$$\Delta P_k = (P_k - \overline{P}) \cdot \sqrt{\frac{N}{N-1}}, \tag{3}$$

where $\Delta P_k$ represents the deviation of each individual parameter $P_k$ from the weighted average $\overline{P}$, and $N$ is the number of observations for that star. These differences serve as a measure of the internal uncertainty of each parameter. To visualize the relationship between $\Delta P$ and the S/N, we plotted scatter diagrams for each parameter, as shown in Figure 3. According to Figure 3, the uncertainty of parameters reduces with the S/N increasing. At S/N > 50, the scatter tends to settle toward a constant value, and the errors on all the parameters are small enough for assessing a high data quality.

To minimize the impact of variable stars or outliers on the evaluation of results, we applied a robust filtering process. We excluded data points that deviated by more than 3 s.d. from the median and iteratively repeated this process three times. In particular, for RV measurements, we also excluded the spectra

[14] The radius of 3.″7 was adopted on the basis of the fiber pointing precision (0.″4) and the 3.″3 diameter of the fiber (W. Zong et al. 2018).

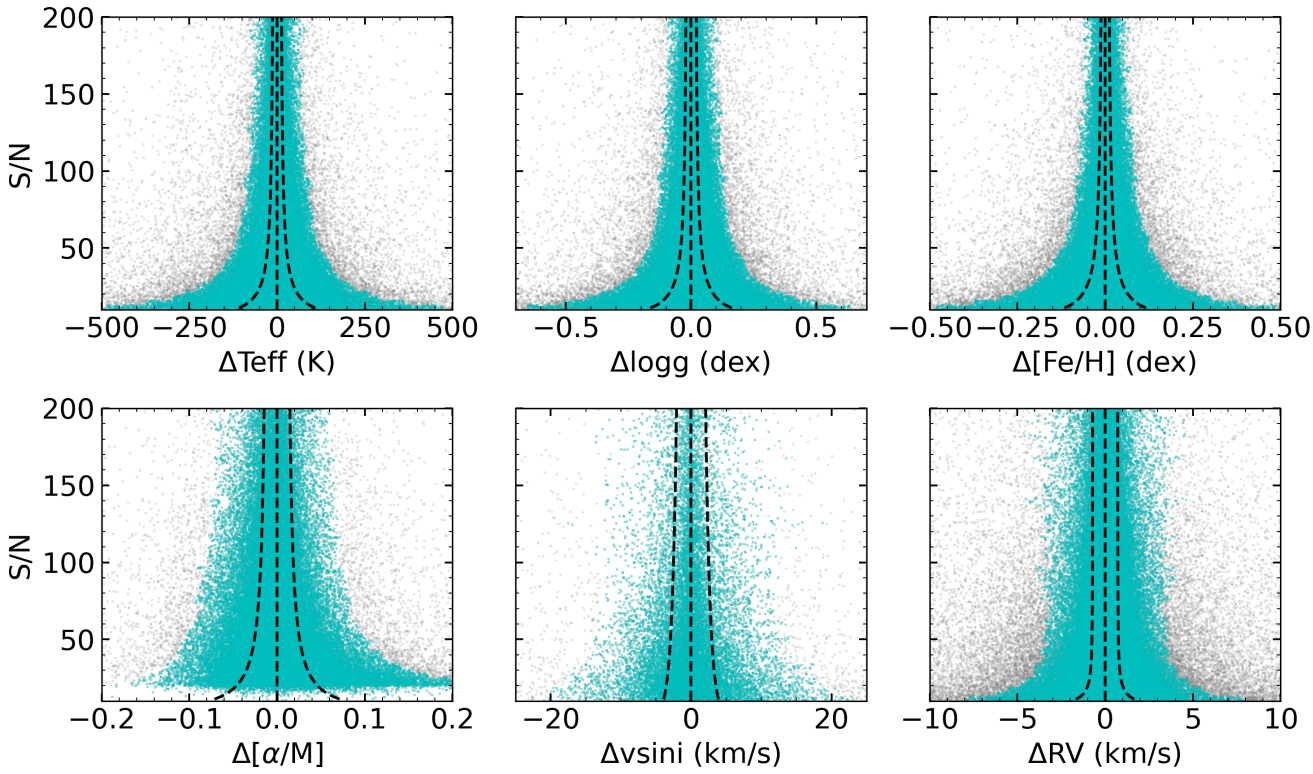


**Figure 3.** S/N vs. internal uncertainties for the five parameters $T_{\rm eff}$, log $g$, [$\alpha/M$], RV, and $v \sin i$. Gray points represent data identified as outliers, while cyan points correspond to data retained after filtering. The black dashed vertical line indicates the zero-point on the $x$-axis, and the black dashed curves on either side represent the fitted relationship between $\Delta P$ and S/N, as modeled by Equation (4).

of RV variable stars identified by the selection described in Section 4.3. The gray points in Figure 3 represent the data identified as outliers, while the cyan points correspond to the data retained after filtering. For all parameters, the cyan points account for more than 92% of the total data, indicating that the filtered data set is highly representative of the overall sample.

To quantify the relationship between $\Delta P$ and S/N, we applied a fit to the filtered data using Equation (4) from Paper I:

$$\sigma_P = a \cdot x^b + c, \tag{4}$$

where $x$ represents the S/N. The fitting coefficients $a$, $b$, and $c$, which characterize this relationship, are provided in Table 3 for each spectral parameter, including $T_{\rm eff}$, log $g$, [Fe/H], [$\alpha/M$], RV, and $v \sin i$. The right side of Table 3 displays the estimated internal errors at S/N values of 10, 20, and 50. As expected, internal errors decrease as S/N increases, stabilizing once the S/N exceeds 50, which indicates that higher-quality spectra yield more reliable parameter estimates in general. For example, the error in $T_{\rm eff}$ reduces from 120 K at S/N = 10 to 27 K at S/N = 50, with similar trends observed for other parameters such as log $g$ and [Fe/H]. The measurement uncertainties for $T_{\rm eff}$ in Paper I are reported as 101 K at S/N = 10 and 29 K at S/N = 50, which aligns well with the uncertainties obtained in this study, providing further validation of the parameter uncertainty estimates. When the S/N reaches 20, the typical measurement uncertainties for $T_{\rm eff}$, log $g$, [Fe/H], [$\alpha$/M], RV, and $v \sin i$ are approximately 59 K, 0.09 dex, 0.06 dex, 0.05 dex, 0.99 km s$^{-1}$, and 3.5 km s$^{-1}$, respectively. Based on this, we consider S/N $\geqslant$ 20 as the threshold for high-quality and reliable parameter estimates in our data set.

**Table 3**
Fit Coefficients for Parameters and Their Measurement Uncertainties at S/Ns = 10, 20, and 50

| | Fitting Coefficients | | | S/N | | |
|---|---|---|---|---|---|---|
| | $a$ | $b$ | $c$ | 10 | 20 | 50 |
| $T_{\rm eff}$ (K) | 1593 | −1.16 | 9.5 | 120 | 59 | 27 |
| log $g$ (dex) | 2.32 | −1.15 | 0.02 | 0.18 | 0.09 | 0.04 |
| [Fe/H] (dex) | 1.42 | −1.07 | 0.01 | 0.13 | 0.06 | 0.03 |
| [$\alpha/M$] (dex) | 0.56 | −0.92 | 0.01 | 0.08 | 0.05 | 0.03 |
| RV (km s$^{-1}$) | 139.51 | −2.08 | 0.71 | 1.9 | 0.99 | 0.75 |
| $v \sin i$ (km s$^{-1}$) | 41.52 | −0.02 | −36.0 | 4.0 | 3.5 | 2.9 |

### 3.3. External Uncertainties in the Parameters of LK-MRS-I

To further assess the accuracy and reliability of the derived parameters, we performed a systematic analysis of their external uncertainties. Following the common practice adopted by J. Wang et al. (2020), we classify stars into giants (log $g$ < 3.5) and dwarfs (log $g$ $\geq$ 3.5) based solely on surface gravity. Applying this threshold to the matched sample from APOGEE and GALAH, we identify a total of 7560 dwarfs and 29,014 giants. This classification enables a more precise evaluation of the external consistency of our stellar parameter estimates. The 17th data release of SDSS (Abdurro'uf et al. 2022) and the third data release of GALAH (S. Buder et al. 2021) provide extensive high-resolution spectroscopic data, making them ideal for cross comparison with the parameters obtained from LK-MRS-I. For stellar

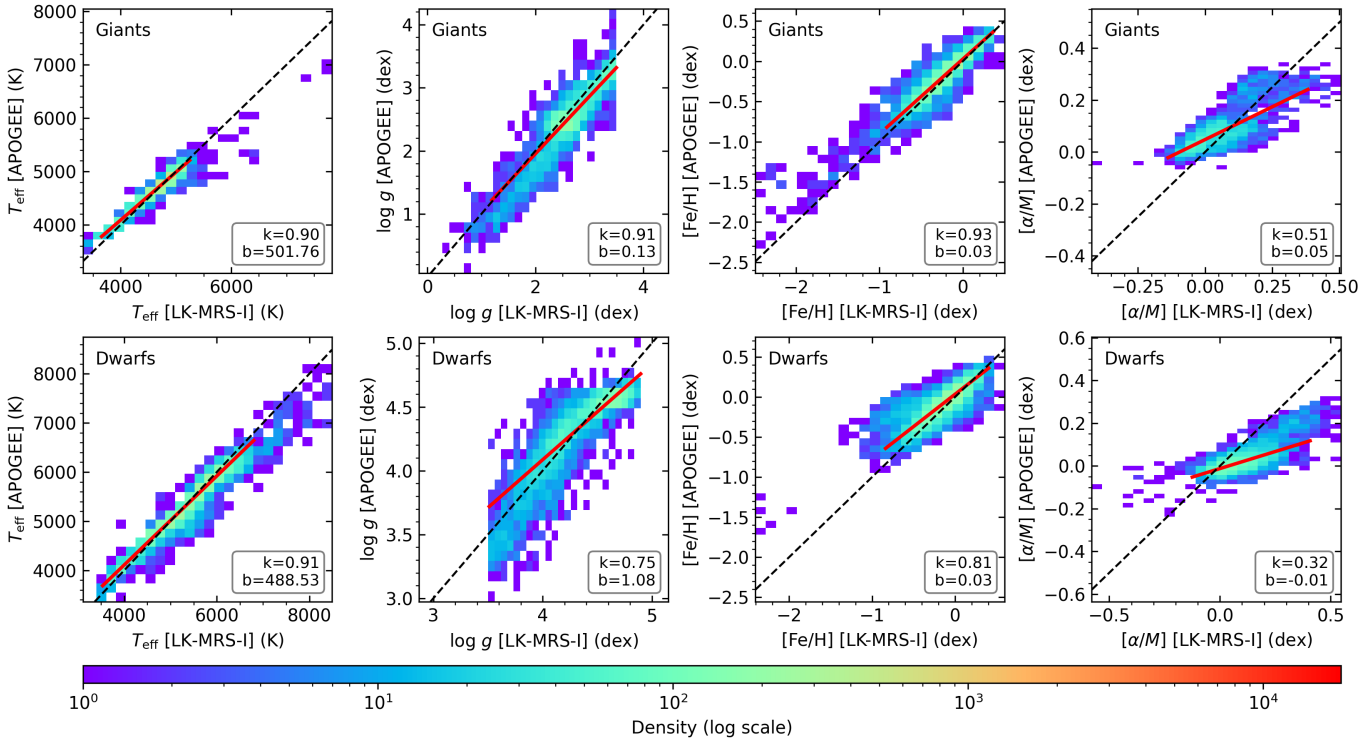


**Figure 4.** Comparison of stellar parameters between LK-MRS-I and APOGEE for giant stars (top row) and dwarf stars (bottom row). Each panel shows a 2D Gaussian density plot, where the color indicates the density of data points. The linear regression (red line) is fitted only to the high-density region that contains 80% of all data points, in order to minimize the influence of outliers. The 1:1 reference line is shown as a black dashed line for comparison. The slope and intercept of the regression line are annotated in the lower-right corner of each panel.

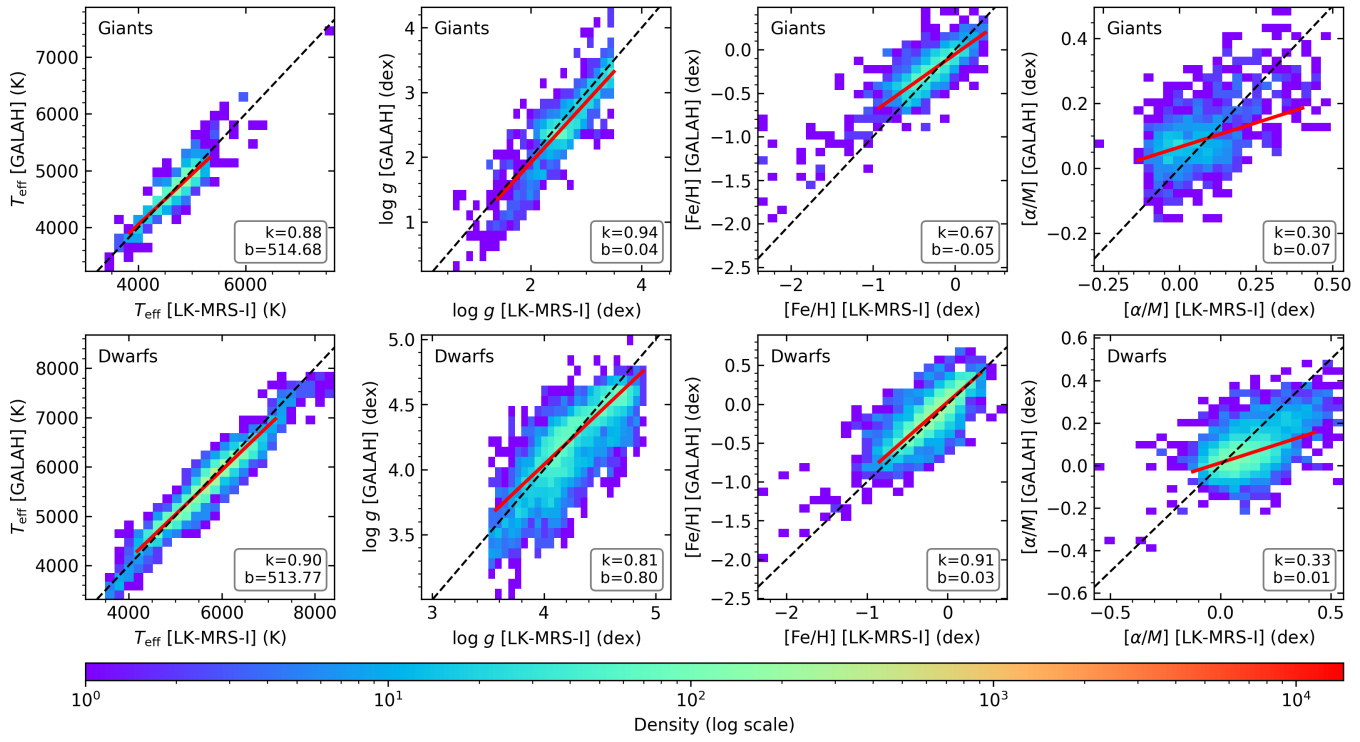


**Figure 5.** Same as Figure 4, but for the comparison between LK-MRS-I and GALAH.

parameters such as $T_{\rm eff}$, log $g$, [Fe/H], $v \sin i$, and [$\alpha$/M], we conduct comparisons separately for dwarfs and giants with the values provided in APOGEE and GALAH. Additionally, Gaia Data Release 3 (Gaia DR3; Gaia Collaboration et al. 2016, 2023) provides high-precision astrometric and RV measurements, which serve as an independent benchmark for validating our RV estimates.

We crossmatched the targets in the processed LK-MRS-I data set with those in APOGEE and GALAH using a uniform crossmatching radius of 3.″7 across all catalogs included in this study. In terms of stellar atmospheric parameters, the crossmatching with APOGEE resulted in 6951 common sources with both $T_{\rm eff}$ and log $g$, 6859 with [Fe/H], and 4530 with [$\alpha$/M]. Similarly, the crossmatch with GALAH yielded 5394 common sources for $T_{\rm eff}$, 5257 for both log $g$ and [Fe/H], and 3694 for [$\alpha$/M], all referring to unique stars in common with the LK-MRS-I data set. Given the limited number of overlapping sources with APOGEE that include $v \sin i$ (949 stars), we did not attempt an external uncertainty analysis for $v \sin i$ in this work. For each atmospheric parameter, we constructed a 2D Gaussian density plot in Figures 4 and 5. Point counts in each bin were convolved with a Gaussian kernel, and the color scale encodes the logarithmic density. To minimize the impact of sparsely populated outliers, we retained only the pixels that enclose the densest 80 % of the cumulative distribution. A Gaussian-weighted least-squares fit was performed on these high-density pixels; the resulting slope and intercept are printed in the lower-right corner of every panel. The black dashed line marks the 1:1 reference, and the red line displays the final regression for the retained high-density region.

Our statistical analysis of stellar atmospheric parameters derived from LK-MRS-I reveals generally good consistency with external high-resolution spectroscopic surveys, particularly APOGEE and GALAH, for key parameters including $T_{\rm eff}$, log $g$, and [Fe/H]. As illustrated in Figures 4 and 5, the regression slopes for these parameters are mostly close to unity, indicating that LK-MRS-I provides reliable estimates across a wide range of stellar types. This consistency shows a clear dependence on stellar evolutionary stage and survey characteristics. APOGEE's scientific focus on evolved giant stars, coupled with its near-infrared high-resolution spectroscopy ($R \sim$ 22,000), makes its giant star parameters especially robust (J. C. Wilson et al. 2019). As a result, LK-MRS giants exhibit better agreement with APOGEE benchmarks. In contrast, the GALAH survey is designed specifically to target main-sequence stars using optical spectra (470–790 nm), which are more sensitive to effective temperature and surface gravity in dwarfs (S. Buder et al. 2021). Consequently, LK-MRS dwarf star parameters show improved consistency with GALAH data, exhibiting smaller systematic offsets. This multisurvey validation across different evolutionary stages and wavelength regimes demonstrates the broad applicability and reliability of LK-MRS parameter determinations. In contrast, [$\alpha$/M] exhibits significant systematic discrepancies for both stellar types across both surveys. The regression slopes are substantially below unity, reflecting a compressed dynamic range in the LK-MRS-I results. These deviations are likely due to the limited resolution ($R \sim$ 7500) and narrow wavelength coverage of the LAMOST spectrograph, which reduces sensitivity to key $\alpha$-element absorption features such as Mg, Si, and Ca. As a result, $\alpha$-element abundances from LK-MRS-I should be interpreted with caution, particularly in studies requiring precise chemical abundances.

As regards the RV, Figure 6 shows a high level of consistency between LK-MRS-I and the reference data sets (Gaia, APOGEE, and GALAH), with regression slopes all close to unity for both giants and dwarfs. Specifically, the slopes range from 0.994 to 1.000, and the intercepts are all within $\pm 0.6\,{\rm km\,s^{-1}}$, indicating negligible systematic offsets. The residual plots further confirm that most data points lie close to zero residual, suggesting excellent agreement in RV measurements across all data sets. These results demonstrate that the RVs derived from LK-MRS-I are reliable and consistent with those from high-precision surveys.

## 4. Peculiar Stars

### 4.1. Metal-poor Star Candidates

Metal-poor stars play a crucial role in probing the origin of first-generation stars in the Galaxy, tracing element production from supernovae, and examining the metallicity distribution function of the Galactic halo (T. C. Beers & N. Christlieb 2005). To support these investigations, acquiring a large, homogenous sample of stellar metallicities is essential. LK-MRS-I measured the metallicities of 35,614 stars, covering a range from −2.5 to 0.9 dex, as illustrated in Figure 7. The blue bars represent the overall distribution, while the orange and red bars highlight the candidates we identified as metal-poor ($-2.0 \leqslant$ [Fe/H] $\leqslant -1.0$) and very metal-poor ($-2.5 \leqslant$ [Fe/H] $\leqslant -2.0$) stars, numbered 746 and 174, respectively, as labeled "MP" and "VMP" in Table 4. To determine which of these are newly discovered, we crossmatched our candidates with the SIMBAD database (M. Wenger et al. 2000) to check for existing classifications. Among the 174 very metal-poor stars, 131 are newly discovered, while 43 have been previously identified in the literature. Similarly, of the 746 metal-poor stars, 678 are newly identified in this work, and 86 have existing records. The full list of metal-poor and very metal-poor stars is provided in Table 4 in Appendix A, and is also available online in a machine-readable format. The middle inset of Figure 7 zooms in on the metal-poor distribution, and the left inset focuses on the very metal-poor range, providing detailed views of these low-metallicity populations.

It is important to note that the majority of candidates for metal-poor stars or very metal-poor stars fall into the F, G, and K types. This is primarily because LASP offers limited spectral templates, only providing parameters for late-A-type, F-type, G-type, and K-type stars (A. L. Luo et al. 2015). Given that our spectra have a medium resolution (approximately 7500), we can only classify these stars as candidates for metal-poor stars or very metal-poor stars. For instance, in our work, EPIC 220387907 is identified as a candidate for a very metal-poor star with an [Fe/H] value of −2.25. However, although A. Abohalima & A. Frebel (2018) also identify it as a very metal-poor star, the [Fe/H] value was given as −2.75. Therefore, further confirmation is required for these candidates of metal-poor stars. Most candidates for metal-poor stars have a magnitude below 15.0 mag, making them suitable for high-resolution follow-up observations with ground-based telescopes, which would enable further confirmation.

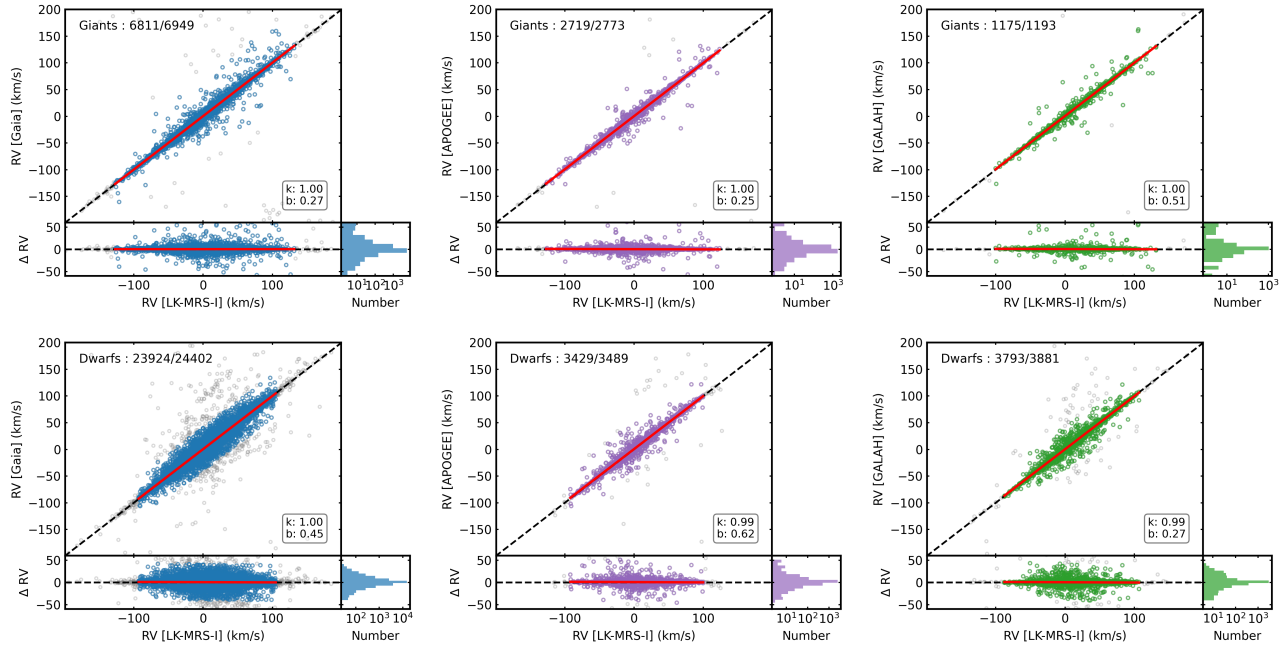


**Figure 6.** Comparison of RVs in the LK-MRS project for giants (top row) and dwarfs (bottom row). Each column corresponds to a survey (from left to right: Gaia, APOGEE, and GALAH). For each panel group, the top-left plot shows the RV comparison between LK-MRS-I and the external reference; the bottom-left plot shows the residuals (ΔRV); and the bottom-right plot displays the histogram of residuals. The black dashed line indicates the one-to-one relation, while the red solid line represents the linear regression fit to the selected data. Mean and rms values of residuals are indicated in each plot.

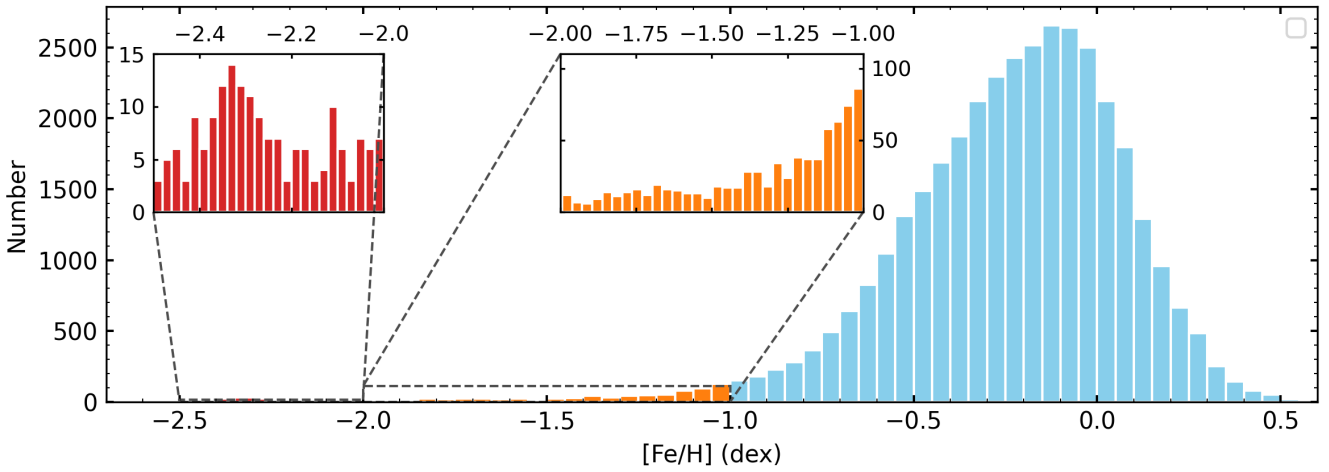


**Figure 7.** The histogram shows the distribution of stellar metallicities [Fe/H] for 35,614 stars measured by LK-MRS-I. The blue bars represent the overall metallicity distribution, while the orange and red bars highlight metal-poor ($-2.0 \leqslant$ [Fe/H] $\leqslant -1.0$) and very metal-poor ($-2.5 \leqslant$ [Fe/H] $\leqslant -2.0$) star candidates, respectively. The inset in the middle provides a closer view of the metal-poor range, while the inset on the left zooms in on the very metal-poor range.

### *4.2. High-velocity Star Candidates*

High-velocity stars, known for their exceptional high speeds and unusual trajectories, have become key subjects in astronomical research (Y. B. Li et al. 2021). LK-MRS-I conducted 161,270 RV measurements of 34,444 stars, covering a velocity range of $-260$ to 350 km s$^{-1}$.

To identify high-velocity stars, we combined the proper motion and positional information provided by the Gaia DR3 with the RV measurements from LK-MRS. Utilizing the `astropy` package (Astropy Collaboration et al. 2022), we transformed these observational data into the three-dimensional Cartesian velocity components ($U$, $V$, $W$). The total velocity, $V_G$, was then calculated as the square root of the sum of the squares of these velocity components. Furthermore, we employed the `Galpy` package (J. Bovy 2015), to model the Galactic escape velocity curve, which is represented as a blue line in Figure 8. The orange line in Figure 8, representing 70% of the escape velocity, acts as a boundary for distinguishing different velocity regimes of high-velocity stars (J. Liao et al. 2024).

Comparing the $V_G$ velocities of 34,444 stars from LK-MRS-I with the Galactic escape velocity, we identified one star whose velocity exceeds this threshold. This star, known as KIC 7881304, has been classified as a long-period variable by J. Yu et al. (2020). Seven LAMOST-MRS spectra indicate a variable RV ranging from 181.8 to 349.2 km s$^{-1}$. These seven measurements are shown as open circles in Figure 8, among which five exceed the Galactic escape velocity. Based on this,

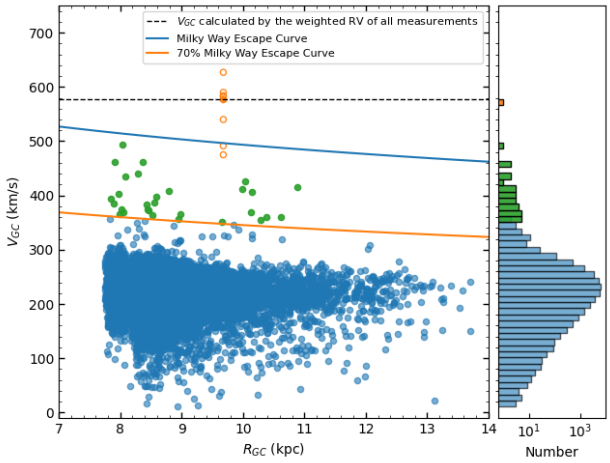


**Figure 8.** The figure illustrates the distribution of stars as a function of their Galactocentric radial distance ($R_{GC}$) and total velocity ($V_{GC}$). The blue curve represents the Galactic escape velocity, while the orange curve marks 70% of this threshold. The open circles indicate the seven individual RV measurements of KIC 7881304, each converted to a corresponding $V_{GC}$ value. The solid dots denote the $V_{GC}$ value derived from the weighted mean RV of KIC 7881304, and the dashed line highlights this representative velocity. The histogram on the right presents the overall distribution of $V_{GC}$ values.

we consider KIC 7881304 a possible unbound high-velocity candidate. It is labeled as "unbound" in Table 2. In addition, 29 stars were found to be moving faster than 70% of the Milky Way's escape velocity. Hence, they were classified as possible candidates for bound high-velocity stars. These 29 stars are labeled as "bound" in Table 2. We crossmatched these candidates with the SIMBAD database to assess whether they were previously known. Among them, 26 of the 29 bound high-velocity stars are newly discovered in this work, while the remaining three have been identified in previous surveys. A detailed list of these 30 high-velocity star candidates, including their RV, $V_{G,}$ and classifications, is provided in Table 5 in Appendix B. Compared with metal-poor stars, we found that most of these 30 high-velocity star candidates exhibit low metallicity, including nine metal-poor stars and 18 very metal-poor stars. However, the final confirmation of these high-velocity star candidates requires further investigations, along with additional observational data and theoretical modeling to ensure a comprehensive and accurate analysis.

### 4.3. RV Variable Star Candidates

RV curves are useful in astronomical research, including recognizing and studying spectroscopic multiple systems (M. Castro-Tapia et al. 2024; T. Pawar et al. 2024), such as binaries, triple stars, etc., identifying modes of pulsating stars (V. Hocdé et al. 2024), and more. Building on the significance of RV curves in stellar analysis, we focus on identifying stars with RV variations using the TD spectra from LK-MRS-I. To ensure a robust identification of the candidates, we applied a selection criterion requiring the standard deviation of RV measurements to exceed 3 times the mean RV uncertainty. Using this threshold, we identified a sample of 2333 candidates exhibiting significant RV variability out of 34,468 stars, corresponding to ∼6.8% of the total population. These stars are labeled as "RVV" in Table 2, and a complete record of their individual RV measurements is provided in Appendix C (Table 6). Additionally, we indicate whether each star is classified as a periodic variable in our later analysis.

Among these candidates, some stars also have photometric data from the Kepler, K2 missions, or TESS (G. R. Ricker et al. 2014), facilitating further classification. By cross-matching the RV variability candidates with the Kepler, K2, and TESS photometric database (STcSI 2018; MAST Team 2021a, 2021b), we found that 1088 out of the 2333 variable star candidates have Kepler/K2 photometric data, 1709 out of the 2333 variable star candidates have TESS photometric data. For these stars, we applied the Lomb–Scargle periodogram to extract periodic features from their light curves and calculated the S/N of the peak frequencies. Using a threshold S/N value of 5.6 (W. Zong et al. 2016), we successfully identified 371 periodic variables.

We further analyzed these 371 stars by examining their light curves, periodograms, and spectroscopic parameters to classify their variability types, with reference to the Variable Star Index catalog (C. L. Watson et al. 2006) and the variable star catalog from Gaia DR3 (Gaia Collaboration 2022) during the classification process. Among them, 194 are newly reported in this work, while 177 had been previously documented in the literature, as determined through crossmatching with the SIMBAD database. Our analysis revealed a diverse range of variable stars, including 76 eclipsing binaries, 11 $\delta$ Scuti variables, 69 $\gamma$ Doradus variables, 21 hybrid $\gamma$ Doradus and $\delta$ Scuti variables, 19 red giants with solar-like oscillations, four RR Lyrae variables, 19 RS Canum Venaticorum variables, and 146 rotating variable stars. The rotating variable stars include those modulated by starspots, stars exhibiting flares, and ellipsoidal variables. Since a single star may exhibit multiple phenomena, such as both starspots and flares, we collectively refer to stars whose brightness varies periodically due to rotation as rotating variable stars. Moreover, we identified six stars whose variability types remain uncertain. We note that in a few cases, our classification differs from that reported in previous surveys. These discrepancies likely arise from the use of different data sources (e.g., spectral resolution, temporal coverage). Therefore, we regard these classifications as candidate types, and recommend that more comprehensive analyses—including high-precision photometry, spectroscopy, and long-term monitoring—be conducted to confirm their true variability nature.

Using the parallaxes and apparent magnitudes provided by Gaia, along with the parameters from LK-MRS-I, we calculated the absolute magnitudes of these stars. Their positions on the effective temperature versus absolute magnitude diagram ($T_{\rm eff}$ versus $M_G$) are shown in Figure 9. The dashed blue belt represents the observational $\delta$ Sct instability strip (IS; S. J. Murphy et al. 2019), while the green belt indicates the theoretical $\delta$ Sct IS (M. A. Dupret et al. 2005). The dotted blue belt within the $\delta$ Sct IS corresponds to the theoretical $\gamma$ Dor IS (M. A. Dupret et al. 2005). The black curves represent the stellar evolutionary tracks for masses of 0.4, 0.8, 1.2, 2.0, and 2.8 $M_\odot$ from MIST (J. Choi et al. 2016; A. Dotter 2016; B. Paxton et al. 2011, 2013, 2015). Although extinction corrections were applied to the magnitudes of these stars using the `dustmap` Python package (G. M. Green 2018), a subset of $\gamma$ Doradus stars remains slightly offset from the theoretical instability strip. This displacement, along with the misplacement of some red giants and RS CVn stars in the parameter space, likely stems from residual uncertainties in extinction corrections or potential systematic errors in stellar parameter determinations. The classified variable stars are

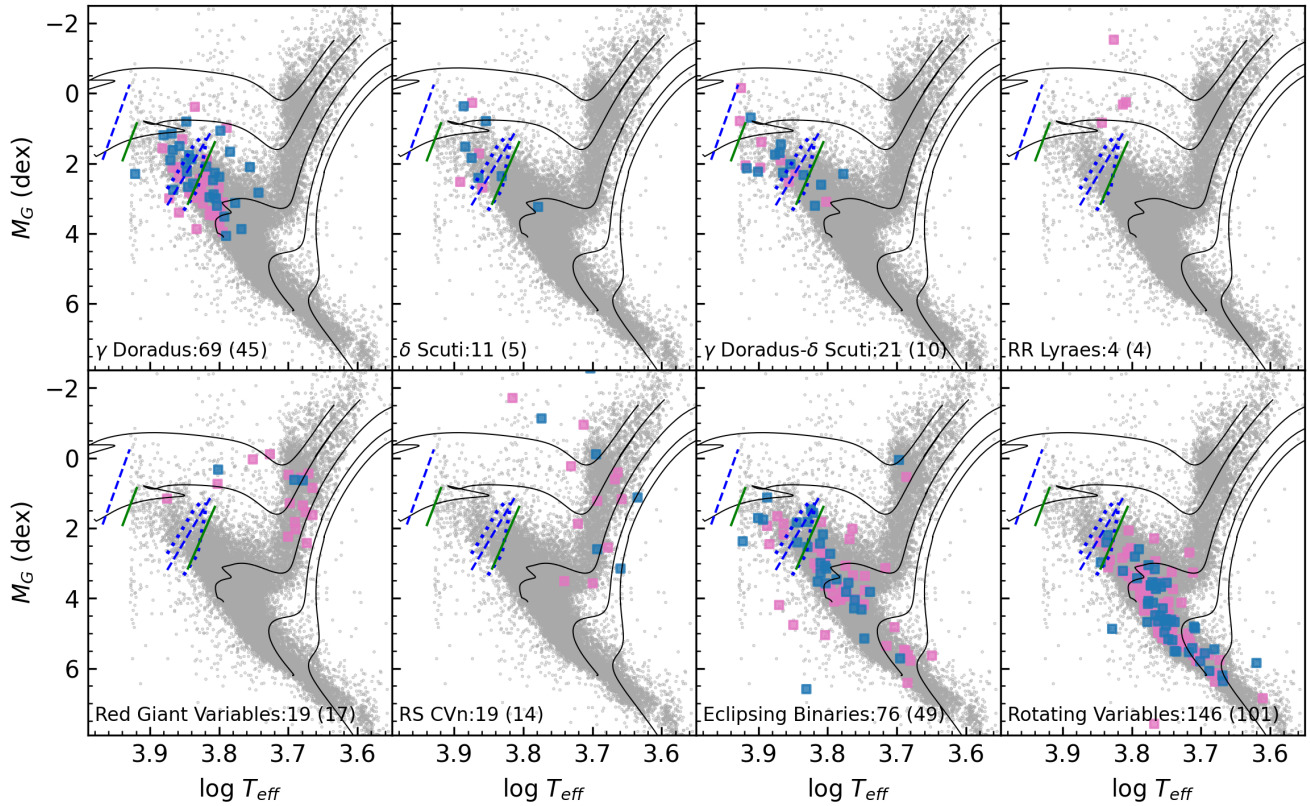


**Figure 9.** Effective temperature vs. absolute magnitude diagram ($T_{\rm eff}$ vs. $M_G$) for variable stars identified in the LK-MRS-I survey. The observational $\delta$ Sct IS is shown as a blue dashed line, the theoretical $\delta$ Sct IS as a green band, and the $\gamma$ Dor IS as a blue dotted line. Black curves represent MIST evolutionary tracks for stellar masses from 0.4 to 2.8 $M_{\odot}$. Gray background points correspond to all LK-MRS-I targets. Variable stars classified by Kepler/K2 and TESS are marked with filled pink and light blue squares, respectively, with their types annotated in the figure. The total number of classified variables is also indicated in each panel, with the number contributed by Kepler/K2 shown in parentheses.

denoted by colored markers: pink squares represent variables identified through Kepler/K2 light curve analysis (with their counts indicated parenthetically), while light blue squares correspond to those classified using TESS photometric data. These results demonstrate that the LK-MRS-I survey not only establishes a crucial benchmark for future asteroseismic investigations but also provides essential constraints for modeling stellar variability mechanisms across different evolutionary stages.

## 5. Summary

As part of the second phase of LAMOST, LK-MRS-I has been conducting a 5 yr TD spectroscopic observation campaign since 2018 September, focusing on 20 plates in the Kepler and K2 fields. During this period, we obtained 3,531,785 spectra of 49,310 stars. The LASP pipeline analyzed the coadded spectra using various spectral templates, calculating $T_{\rm eff}$, $\log g$, and [Fe/H] for 170,637 spectra, RV for 161,270 spectra, $v \sin i$ for 23,810 spectra, and $[\alpha/M]$ for 94,075 spectra through template matching.

We computed the weighted averages of the stellar parameters from LASP for 36,588 stars, along with their associated uncertainties. The results are summarized in Table 2. To assess the measurement uncertainties, we calculated the differences between individual spectra and their corresponding weighted mean values, and examined their relationship with the S/N. At S/N = 10, the measurement uncertainties are as follows: 120 K for $T_{\rm eff}$, 0.18 dex for $\log g$, 0.13 dex for [Fe/H], 0.08 dex for $[\alpha/M]$, 1.9 km s$^{-1}$ for RV, and 4.0 km s$^{-1}$ for $v \sin i$. As the S/N increases, the parameter uncertainties decrease, stabilizing when the S/N exceeds 50 in general. At S/N = 50, the uncertainties are approximately 27 K for $T_{\rm eff}$, 0.04 dex for $\log g$, 0.03 dex for [Fe/H], 0.03 dex for $[\alpha/M]$, 0.75 km s$^{-1}$ for RV, and 2.9 km s$^{-1}$ for $v \sin i$. For an external uncertainty estimate, we compared our results with independent data from Gaia, APOGEE, and GALAH. The comparison showed good agreement for RV, $T_{\rm eff}$, $\log g$ and [Fe/H], but systematic offsets were found for $[\alpha/M]$.

With the metallicity information provided by LK-MRS-I, we identified 764 metal-poor star candidates and 174 very metal-poor star candidates. Using the Galactic escape velocity curve, we identified one high-velocity star candidate that is not gravitationally bound to the Milky Way and 29 high-velocity star candidates that are bound. Additionally, we identified 2333 stars with significant RV variations. By combining the photometric and spectroscopic data, we further classified 371 periodic variable star candidates, including 76 binaries, 11 $\delta$ Scuti stars, 69 $\gamma$ Doradus stars, 21 hybrid $\gamma$ Doradus-$\delta$ Scuti variables, 19 red giants, four RR Lyrae variables, 19 RS Canum Venaticorum variables, and 146 rotating variable stars. Based on the available data, we are still unable to determine the variable star type for six stars.

Since 2023 September, LK-MRS has officially entered the second 5 yr survey. In 2024 February, the LAMOST official website[15] released an internal test version of the data

[15] https://www.lamost.org/

resources. We are actively organizing and filtering the data collected by LK-MRS, and as astronomical observations progress, new data will be continuously released. We look forward to the scientific community making use of these data sets to drive further advancements in research.

## Acknowledgments

We acknowledge the support from the National Natural Science Foundation of China (NSFC) through the grants 12090040, 12090042, and 12427804, and the science research grants from the China Manned Space Project. This work is supported by the China Manned Space Program with grant No. CMS-CSST-2025-A13, the Tianchi Talent Introduction Plan, and the Central Guidance for Local Science and Technology Development Fund under No. ZYYD2025QY27. Guoshoujing Telescope (LAMOST) is a National Major Scientific Project built by the Chinese Academy of Sciences. H.Y. acknowledges the support from the Youth Innovation Promotion Association of the Chinese Academy of Sciences. Funding for the project has been provided by the National Development and Reform Commission. It is operated and managed by the National Astronomical Observatories, Chinese Academy of Sciences.

## Appendix A
## Parameters of Metal-poor Star Candidates

The observation times, target IDs, positions, [Fe/H], specific classifications, and information on whether they are newly discovered in this work are listed in Table 4 for the metal-poor and very metal-poor star candidates selected in Section 4.1.

**Table 4**
Metal-poor Star Candidates Identified in LK-MRS-I

| Times | UID | Gaia Source | KIC/EPIC | R.A. (deg) | Decl. (deg) | [Fe/H] (dex) | Label | Discovery |
|---|---|---|---|---|---|---|---|---|
| 1 | G16299287415772 | 598414739630537600 | 211344111 | 130.74812 | 10.70665 | −1.33 | MP | Known |
| 1 | G16343607386694 | 605159247034372224 | ⋯ | 133.29913 | 12.93157 | −2.45 | VMP | New |
| 1 | G15632253923687 | 3865499501595685376 | 248633859 | 161.03179 | 6.72897 | −1.10 | MP | New |
| 1 | G14076948140108 | 2080028820098431616 | ⋯ | 295.39068 | 46.07732 | −2.05 | VMP | New |
| 2 | G16330175937848 | 689476876759791360 | 212170836 | 132.26083 | 23.50690 | −1.07 | MP | New |
| 1 | G16713619459999 | 144889557795806848 | ⋯ | 69.24472 | 21.74420 | −2.36 | VMP | New |
| 1 | G16329236204097 | 652853175231968128 | K | 125.90789 | 15.91996 | −1.11 | MP | New |
| 1 | G17073665209151 | 2538128245175162496 | ⋯ | 16.52815 | 1.37751 | −2.18 | VMP | New |
| 1 | G16585545411581 | 147111567716180096 | 247808458 | 72.65588 | 24.46694 | −2.23 | VMP | New |

**Note.** Column (1) provides the number of available spectral parameters for each target. Column (2) presents the UID, while Column (3) gives the Gaia source ID. Column (4) provides the KIC/EPIC identifier (if available; "⋯" denotes no match). Columns (5) and (6) contain the R.A. and decl. in J2000.0 coordinates. Column (7) presents the [Fe/H] metallicity in dex. Column (8) provides the metallicity classification (MP = metal-poor with $-2.0 \lesssim$ [Fe/H] $< -1.0$; VMP = very metal-poor with [Fe/H] $\lesssim -2.0$). Column (9) indicates the discovery status (Known = present in SIMBAD; New = newly recognized in this work).

(This table is available in its entirety in machine-readable form in the online article.)

## Appendix B
## Parameters of High-velocity Star Candidates

The observation times, target IDs, positions, RV, $V_G$, specific classifications, and information on whether they are newly discovered in this work are listed in Table 5 for the high-velocity star candidates selected in Section 4.2.

**Table 5**
High-Velocity Star Candidates Identified in LK-MRS-I

| Times | UID | KIC/EPIC | R.A. (deg) | Decl. (deg) | RV (km s$^{-1}$) | $V_{GC}$ (km s$^{-1}$) | Label | Discovery |
|---|---|---|---|---|---|---|---|---|
| 1 | G14078689694621 | 10796857 | 291.68157 | 48.12203 | 132.45 | 374.02 | Bound | New |
| 4 | G17525854519286 | ⋯ | 55.56701 | 25.26853 | 159.08 | 354.31 | Bound | New |
| 4 | G17525829022163 | ⋯ | 55.93135 | 25.54486 | 261.31 | 356.68 | Bound | New |
| 5 | G14087386039950 | 7612547 | 293.37042 | 43.25230 | 169.08 | 434.35 | Bound | New |
| 12 | L15619442062806 | ⋯ | 158.64312 | 5.56515 | −37.87 | 360.64 | Bound | Known |
| 8 | G17065374200707 | 220496220 | 13.10688 | 6.68008 | 215.77 | 374.40 | Unbound | Known |
| 5 | G14081832652116 | 5953450 | 289.59470 | 41.23543 | −0.02 | 394.47 | Bound | New |
| 3 | G15626569425898 | 248671171 | 157.98600 | 7.64722 | −34.70 | 369.90 | Bound | New |
| 2 | G17075733875360 | ⋯ | 16.36599 | 3.55150 | 96.19 | 351.40 | Bound | New |
| 1 | G16295662579783 | 211440176 | 129.72939 | 12.24899 | −258.68 | 397.15 | Bound | New |

**Note.** Columns (1)–(3) list the number of available spectral parameters for each target, UID, and KIC/EPIC ID (if available). Columns (4)–(5) give J2000 coordinates. Columns (6)–(7) list heliocentric RV and the Galactic standard-of-rest velocity. Column (8) gives the kinematic label, and column (9) indicates whether the star was previously known or newly identified. The full table, including Gaia source IDs, is available online.

(This table is available in its entirety in machine-readable form in the online article.)

## Appendix C
## Parameters of RV Variable Star Candidates

Table 6 presents the spectral information for all radial velocity variable stars identified in Section 4.3. Each star corresponds to multiple spectra, and for each spectrum, the table provides the ID, position, MJD, S/N, RV with its uncertainty, as well as classification and whether the star is newly discovered in this work.

**Table 6**
RV Variable Star Candidates of LK-MRS-I

| UID | R.A. (deg) | Decl. (deg) | MJD (days) | S/N | RV (km s$^{-1}$) | $RV_{error}$ (km s$^{-1}$) | KIC/EPIC | TIC | Label | Discovery |
|---|---|---|---|---|---|---|---|---|---|---|
| G14075814741395 | 288.904419 | 44.520668 | 58624 | 70.17 | −49.97 | 1.13 | ⋯ | 158844295 | gamma | Known |
| G14075814741395 | 288.904419 | 44.520668 | 58645 | 65.61 | −51.98 | 1.18 | ⋯ | 158844295 | gamma | Known |
| G14075814741395 | 288.904419 | 44.520668 | 58269 | 40.98 | −37.12 | 0.62 | ⋯ | 158844295 | gamma | Known |
| G14075814741395 | 288.904419 | 44.520668 | 58266 | 77.94 | −37.27 | 0.66 | ⋯ | 158844295 | gamma | Known |
| G14075814741395 | 288.904419 | 44.520668 | 58643 | 120.28 | −53.10 | 1.18 | ⋯ | 158844295 | gamma | Known |
| L17526106473874 | 57.878652 | 25.140276 | 58829 | 57.86 | −25.75 | 1.41 | 211134060.0 | 84331634 | gamma | New |
| L17526106473874 | 57.878652 | 25.140276 | 58835 | 18.90 | −21.54 | 1.39 | 211134060.0 | 84331634 | gamma | New |
| L17526106473874 | 57.878652 | 25.140276 | 59180 | 42.79 | −14.59 | 1.32 | 211134060.0 | 84331634 | gamma | New |
| L17526106473874 | 57.878652 | 25.140276 | 59189 | 85.94 | −13.35 | 1.33 | 211134060.0 | 84331634 | gamma | New |
| L17526106473874 | 57.878652 | 25.140276 | 58851 | 126.35 | −20.06 | 1.31 | 211134060.0 | 84331634 | gamma | New |

**Note.** Column (1) provides the UID for each target. Columns (2) and (3) list the R.A. and decl. in J2000.0 coordinates. Column (4) contains the modified Julian date (MJD) of the observations. Column (5) gives the S/N. Columns (6) and (7) provide the measured RV and its associated uncertainty. Columns (8) and (9) list the KIC/EPIC and TIC IDs (if available). Column (10) indicates the variability class, and Column (11) specifies the discovery status. The complete table, including Gaia source IDs, is available online.

(This table is available in its entirety in machine-readable form in the online article.)

## ORCID iDs

Mingfeng Qin https://orcid.org/0000-0002-0040-8351
Jian-Ning Fu https://orcid.org/0000-0001-8241-1740
Weikai Zong https://orcid.org/0000-0002-7660-9803
Peter De Cat https://orcid.org/0000-0001-5419-2042
Antonio Frasca https://orcid.org/0000-0002-0474-0896
Tianqi Cang https://orcid.org/0000-0003-3816-7335
Jiangtao Wang https://orcid.org/0000-0002-2316-8194
Jianrong Shi https://orcid.org/0000-0002-0349-7839
Ali Luo https://orcid.org/0000-0001-7865-2648
Hongliang Yan https://orcid.org/0000-0002-8609-3599
R. O. Gray https://orcid.org/0000-0001-7588-0477

## References

Abdurro'uf, Accetta, K., Aerts, C., et al. 2022, ApJS, 259, 35
Abohalima, A., & Frebel, A. 2018, ApJS, 238, 36
Astropy Collaboration, Price-Whelan, A. M., Lim, P. L., et al. 2022, ApJ, 935, 167
Barentsen, G., Hedges, C., Saunders, N., et al. 2018, arXiv:1810.12554
Beers, T. C., & Christlieb, N. 2005, ARA&A, 43, 531
Borucki, W. J., Koch, D., Basri, G., et al. 2010, Sci, 327, 977
Bovy, J. 2015, ApJS, 216, 29
Buder, S., Sharma, S., Kos, J., et al. 2021, MNRAS, 506, 150
Castro-Tapia, M., Aguilera-Gómez, C., & Chanamé, J. 2024, A&A, 690, A367
Choi, J., Dotter, A., Conroy, C., et al. 2016, ApJ, 823, 102
De Cat, P., Fu, J. N., Ren, A. B., et al. 2015, ApJS, 220, 19
Dotter, A. 2016, ApJS, 222, 8
Dupret, M. A., Grigahcène, A., Garrido, R., Gabriel, M., & Scuflaire, R. 2005, A&A, 435, 927
Frasca, A., Molenda-Żakowicz, J., Alonso-Santiago, J., et al. 2022, A&A, 664, A78
Frasca, A., Zhang, J. Y., Alonso-Santiago, J., et al. 2025, A&A, 698, A7
Fu, J.-N., De Cat, P., Zong, W., et al. 2020, RAA, 20, 167
Gaia Collaboration 2022, yCat, 1355, 0
Gaia Collaboration, Prusti, T., de Bruijne, J., H., J., et al. 2016, A&A, 595, A1
Gaia Collaboration, Vallenari, A., Brown, A. G. A., et al. 2023, A&A, 674, A1
Green, G. M. 2018, JOSS, 3, 695
Han, H., Wang, S., Bai, Y., et al. 2023, ApJS, 264, 12
Hocdé, V., Moskalik, P., Gorynya, N. A., et al. 2024, A&A, 689, A224
Howell, S. B., Sobeck, C., Haas, M., et al. 2014, PASP, 126, 398
Jin, M., Fu, J., Zhang, X., et al. 2024, AJ, 168, 280
Li, X., Wang, S., Han, H., et al. 2024, ApJ, 966, 69
Li, X., Wang, S., Zhao, X., et al. 2022, ApJ, 938, 78
Li, Y. B., Luo, A. L., Lu, Y.-J., et al. 2021, ApJS, 252, 3
Liao, J., Du, C., Deng, M., et al. 2024, AJ, 167, 76
Liu, C., Fu, J., Shi, J., et al. 2020, arXiv:2005.07210
Lu, H.-P., Tian, H., Zhang, L.-Y., et al. 2025, ApJL, 978, L32
Luo, A. L., Zhao, Y.-H., Zhao, G., et al. 2015, RAA, 15, 1095
Ma, X. Y., Zong, W., Fu, J. N., et al. 2023, A&A, 680, A11
MAST Team 2021a, TESS Light Curves – All Sectors, MAST, doi:10.17909/T9-NMC8-F686
MAST Team 2021b, TESS "Fast" Light Curves – All Sectors, MAST, doi:10.17909/T9-ST5G-3177
Mathur, S., Claytor, Z. R., Santos, Â. R. G., et al. 2023, ApJ, 952, 131
Murphy, S. J., Hey, D., Van Reeth, T., & Bedding, T. R. 2019, MNRAS, 485, 2380
Pan, Y., Frasca, A., Wang, J.-X., Fu, J.-N., & Zhang, X.-B. 2024, AJ, 168, 253
Pan, Y., Fu, J.-N., Zong, W., et al. 2020, ApJ, 905, 67
Pawar, T., Hełminiak, K. G., Moharana, A., et al. 2024, A&A, 691, A101
Paxton, B., Bildsten, L., Dotter, A., et al. 2011, ApJS, 192, 3
Paxton, B., Cantiello, M., Arras, P., et al. 2013, ApJS, 208, 4
Paxton, B., Marchant, P., Schwab, J., et al. 2015, ApJS, 220, 15
Pinsonneault, M. H., Elsworth, Y., Epstein, C., et al. 2014, ApJS, 215, 19
Pinsonneault, M. H., Elsworth, Y. P., Tayar, J., et al. 2018, ApJS, 239, 32
Ricker, G. R., Winn, J. N., Vanderspek, R., et al. 2014, Proc. SPIE, 9143, 914320
Rothermich, A., Faherty, J. K., Bardalez-Gagliuffi, D., et al. 2024, AJ, 167, 253
Serenelli, A., Johnson, J., Huber, D., et al. 2017, ApJS, 233, 23
STScI 2011, Kepler/KIC, MAST, doi:10.17909/T9059R
STScI 2016a, Kepler/EPIC, MAST, doi:10.17909/T93W28
STScI 2016b, Kepler LC+SC, Q0-Q17, MAST, doi:10.17909/T98304
STScI 2016c, K2 Light Curves (all), MAST, doi:10.17909/T9WS3R
STsCI 2018, TESS Input Catalog and Candidate Target List, MAST, doi:10.17909/FWDT-2X66
Wang, J., Fu, J.-N., Zong, W., Wang, J., & Zhang, B. 2021, MNRAS, 506, 6117
Wang, J., Fu, J.-N., Zong, W., et al. 2020, ApJS, 251, 27
Wang, J., Pan, Y., Fu, J., et al. 2024, A&A, 690, A201
Wang, R., Luo, A. L., Chen, J. J., et al. 2019, ApJS, 244, 27
Wang, R., Luo, A. L., Zhang, S., et al. 2023, ApJS, 266, 40
Watson, C. L., Henden, A. A., & Price, A. 2006, SASS, 25, 47
Wenger, M., Ochsenbein, F., Egret, D., et al. 2000, A&AS, 143, 9
Wilson, J. C., Hearty, F. R., Skrutskie, M. F., et al. 2019, PASP, 131, 055001
Wittenmyer, R. A., Sharma, S., Stello, D., et al. 2018, AJ, 155, 84
Worley, C. C., Jofré, P., Rendle, B., et al. 2020, A&A, 643, A83
Yan, H., Li, H., Wang, S., et al. 2022, Innov, 3, 100224
Yu, J., Bedding, T. R., Stello, D., et al. 2020, MNRAS, 493, 1388
Zhang, B., Jing, Y.-J., Yang, F., et al. 2022, ApJS, 258, 26
Zhang, B., Li, J., Yang, F., et al. 2021, ApJS, 256, 14
Zhao, G., Zhao, Y.-H., Chu, Y.-Q., Jing, Y.-P., & Deng, L.-C. 2012, RAA, 12, 723
Zong, P., Fu, J.-N., Su, J., et al. 2024, AJ, 167, 227
Zong, W., Charpinet, S., Vauclair, G., Giammichele, N., & Van Grootel, V. 2016, A&A, 585, A22
Zong, W., Fu, J.-N., De Cat, P., et al. 2018, ApJS, 238, 30
Zong, W., Fu, J.-N., De Cat, P., et al. 2020, ApJS, 251, 15
Zuo, F., Luo, A. L., Du, B., et al. 2024, ApJS, 271, 4